

# A multifrequency study of giant radio sources

## I. Low-frequency Giant Metrewave Radio Telescope observations of selected sources

C. Konar<sup>1,2\*</sup>, M. Jamrozy<sup>3</sup>, D. J. Saikia<sup>1</sup> and J. Machalski<sup>3</sup>

<sup>1</sup> *National Centre for Radio Astrophysics, TIFR, Pune University Campus, Post Bag 3, Pune 411 007, India*

<sup>2</sup> *Inter-University Centre for Astronomy and Astrophysics, Pune University Campus, Post Bag 4, Pune 411 007, India*

<sup>3</sup> *Obserwatorium Astronomiczne, Uniwersytet Jagielloński, ul. Orla 171, 30244 Kraków, Poland*

Accepted. Received

### ABSTRACT

We present low-frequency observations with the Giant Metrewave Radio Telescope (GMRT) of a sample of giant radio sources (GRSs), and high-frequency observations of three of these sources with the Very Large Array (VLA). From multifrequency observations of the lobes we estimate the magnetic field strengths using three different approaches, and show that these differ at most by a factor of  $\sim 3$ . For these large radio sources the inverse-Compton losses usually dominate over synchrotron losses when estimates of the classical minimum energy magnetic field are used, consistent with earlier studies. However, this is often not true if the magnetic fields are close to the values estimated using the formalism of Beck & Krause. We also examine the spectral indices of the cores and any evidence of recurrent activity in these sources. We probe the environment using the symmetry parameters of these sources and suggest that their environments are often asymmetric on scales of  $\sim 1$  Mpc, consistent with earlier studies.

**Key words:** galaxies: active – galaxies: jets – galaxies: nuclei – quasars: general – radio continuum: galaxies

### 1 INTRODUCTION

Giant radio sources (GRSs) are defined to be those which have a projected linear size  $\gtrsim 1$  Mpc ( $H_0=71$  km s<sup>-1</sup> Mpc<sup>-1</sup>,  $\Omega_m=0.27$ ,  $\Omega_{vac}=0.73$ , Spergel et al. 2003). These are useful for studying a number of astrophysical problems which include probing the late stages of evolution of radio sources, constraining orientation-dependent unified schemes and probing the intergalactic medium at different redshifts (e.g. Subrahmanyan & Saripalli 1993; Subrahmanyan, Saripalli & Hunstead 1996; Mack et al. 1998; Ishwara-Chandra & Saikia 1999; Kaiser & Alexander 1999; Blundell, Rawlings & Willott 1999 and references therein; Schoenmakers 1999; Schoenmakers et al. 2000, 2001). In addition, these sources are useful for studying the effects of electron energy loss in the lobe plasma due to inverse-Compton scattering with the Cosmic Microwave Background Radiation (CMBR) photons at different redshifts (e.g. Konar et al. 2004) and spectral as well as dynamical ageing analyses to understand the evolution of the sources (e.g. Konar et al. 2006; Machalski et

al. 2007). Although the number of GRSs published in the literature has increased significantly, there is still a dearth of GRSs with sizes  $\gtrsim 2$  Mpc and at redshifts  $\gtrsim 1$ . The largest known radio source is 3C236 (Strom & Willis 1980) with a size of approximately 4 Mpc while the highest redshift GRS known so far is 4C 39.24 at a redshift of 1.88 (Law-Green et al. 1995).

We have selected a representative, but somewhat heterogeneous sample of 10 edge-brightened, large radio sources spread over about two decades in luminosity and lying between redshifts of  $\sim 0.1$  and 0.8 for observations with the Giant Metrewave Radio Telescope (GMRT) and the Very Large Array (VLA) over a large frequency range. Seven of the ten sources are from the sample of GRSs studied by Machalski, Jamrozy & Zola (2001) and Machalski et al. (2006, hereinafter referred to as MJZK), while the remaining three are from our earlier study (Konar et al. 2004). The Machalski et al. sample was compiled from the NRAO VLA Sky Survey (NVSS, Condon et al. 1998) and the Faint Images of the Radio Sky at Twenty-centimeters (FIRST) survey (Becker, White & Helfand 1995). Due to limitations of observing time we restricted our study to a sample of ten sources. The objectives of these observations are to estimate

\* E-mail: chiranjib@iucaa.ernet.in (CK), jamrozy@oa.uj.edu.pl (MJ), djs@ncra.tifr.res.in (DJS), machalsk@oa.uj.edu.pl (JM)

their spectral ages, injection spectral indices ( $\alpha_{\text{inj}}$ ), and also examine the range of magnetic field estimates using different formalisms and their effect on the estimates of the spectral ages. It is worth noting here that a determination of the spectra of the lobes over a large frequency range from our observations would help get reliable estimates of the physical parameters of the lobes such as their magnetic fields. We also explore any evidence of recurrent activity and attempt to probe the environments of these sources on Mpc scales using their symmetry parameters.

With the current cosmological parameters, eight of the 10 sources in our sample have projected linear sizes  $\gtrsim 1$  Mpc. In this paper (Paper I) we report GMRT observations of nine of these sources at a number of frequencies ranging from  $\sim 240$  to 1300 MHz, and also VLA observations for three of the sources, namely J1313+6937 at 4873 MHz, J1604+3731 at 4860 and 9040 MHz and J1702+4217 at 4860 and 8440 MHz. GMRT images of J1343+3758 at 316 and 604 MHz are presented here, although the source has been studied earlier by Jamrozy et al. (2005). The observations presented here for this sample provide information on their low-frequency emission and help establish the spectra of the lobes over a large frequency range. In this paper these spectra have been used to estimate the magnetic fields of the lobes using three different formalisms to understand the possible range of these values, make a comparative study of the relative importance of inverse Compton and synchrotron losses, and explore some of the consequences. We also discuss the core strengths and symmetry parameters of these sources to probe their environments and compare with earlier studies.

In a forthcoming paper (Jamrozy et al. 2007; hereinafter referred to as Paper II) we use the results of our observations to estimate the spectral ages and injection spectral indices of these sources and examine possible correlations of  $\alpha_{\text{inj}}$  with luminosity, redshift and size.

## 2 OBSERVATIONS AND ANALYSES

Both the GMRT and the VLA observations were made in the standard fashion, with each target source observations interspersed with observations of the phase calibrator. The primary flux density calibrator was any one of 3C48, 3C147 and 3C286 with all flux densities being on the scale of Baars et al. (1977). The total observing time on the source is about a few hours for the GMRT observations while for the VLA observations the time on source ranges from 10 to 20 minutes. The low-frequency GMRT data were sometimes significantly affected by radio frequency interference, and these data were flagged. All the data were analysed in the standard fashion using the NRAO AIPS package. All the data were self calibrated to produce the best possible images

The observing log for both the GMRT and the VLA observations is given in Table 1 which is arranged as follows. Columns 1 and 2 show the name of the telescope, and the array configuration for the VLA observations; column 3 shows the frequency of the observations in MHz, while columns 4 and 5 list the sources observed and the dates of the observations respectively.

**Table 1.** Observing log

Telescope	Array Conf.	Obs. Freq. MHz	Sources	Obs. Date
(1)	(2)	(3)	(4)	(5)
GMRT		241	J1155+4029	2005 Mar 16
GMRT		239	J1604+3438	2005 Dec 28
GMRT		334	J0912+3510	2003 Sep 20
GMRT		316	J0927+3510	2003 Sep 20
GMRT		334	J1155+4029	2005 Dec 25
GMRT		316	J1343+3758	2003 Sep 20
GMRT		334	J1604+3731	2006 Mar 09
GMRT		334	J1604+3438	2006 Apr 04
GMRT		334	J2312+1845	2005 Sep 08
GMRT		604	J0720+2837	2003 Sep 05
GMRT		606	J0912+3510	2003 Sep 05
GMRT		606	J0927+3510	2003 Sep 06
GMRT		604	J1343+3758	2003 Sep 06
GMRT		605	J1155+4029	2005 Mar 16
GMRT		614	J1604+3438	2005 Dec 28
GMRT		613	J1604+3731	2004 Jan 01
GMRT		602	J1702+4217	2004 Jan 17
GMRT		1289	J1604+3731	2006 Jan 01
GMRT		1288	J1702+4217	2005 Dec 04
GMRT		1258	J1155+4029	2005 Nov 30
GMRT		1265	J1604+3438	2006 Jul 12
VLA <sup>a</sup>	D	4860	J1604+3731	1993 Dec 23
VLA <sup>a</sup>	D	4860	J1702+4217	1993 Dec 23
VLA	D	4873	J1313+6937	2000 Aug 18
VLA <sup>a</sup>	D	8440	J1702+4217	1993 Dec 23
VLA <sup>a</sup>	D	9040	J1604+3731	1993 Dec 23

<sup>a</sup> unpublished archival data from the VLA

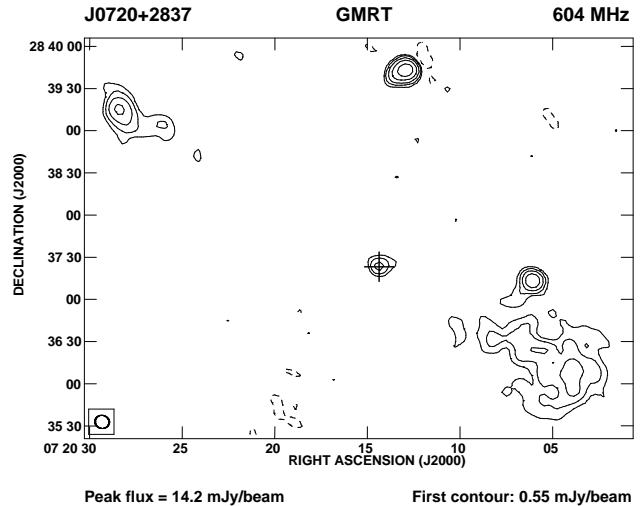


**Figure 1.** GMRT image of J0720+2837 at 604 MHz. In this figure as well as in all the other images of the sources, the peak brightness and the first contour level are given below each image. The contour levels are  $-1, 1, 2, 4, 8 \dots$  times the first contour level. In all the images the restoring beam is indicated by an ellipse and the + sign indicates the position of the optical host galaxy.

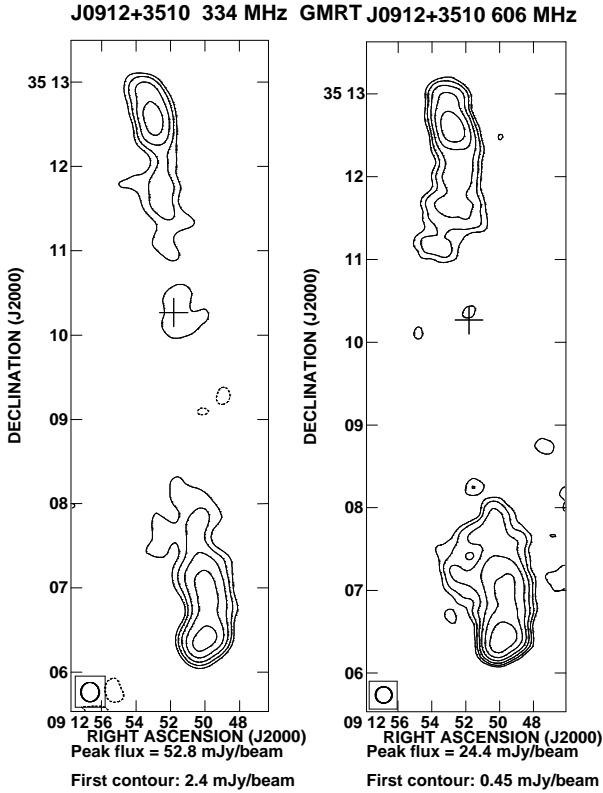


Figure 1 – continued

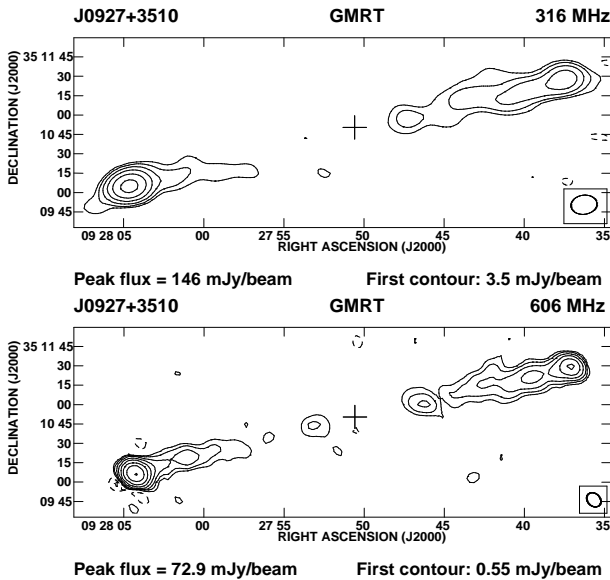


Figure 1 – continued

### 3 OBSERVATIONAL RESULTS

The GMRT images of the sources at the different frequencies are presented in Figure 1, while the observational parameters and some of the observed properties are presented in Table 2, which is arranged as follows. Column 1: Name of the source; column 2: frequency of observations in units of MHz, with the letter G or V representing either GMRT or

VLA observations; columns 3-5: the major and minor axes of the restoring beam in arcsec and its position angle (PA) in degrees; column 6: the rms noise in units of  $\text{mJy beam}^{-1}$ ; column 7: the integrated flux density of the source in mJy estimated by specifying an area enclosing the entire source. We examined the change in flux density by specifying different areas and found the difference to be within a few per cent. The flux densities at different frequencies have been estimated over similar areas. Columns 8, 11 and 14: component designation, where W, E, N, S and C denote the western, eastern, northern, southern and core components respectively; columns 9 and 10, 12 and 13, and 15 and 16: the peak and total flux densities of each of the components in units of  $\text{mJy beam}^{-1}$  and mJy respectively. The core flux densities were sometimes evaluated by imaging the source using the longer spacings so that the core appears reasonably isolated. The superscript  $g$  indicates that the flux densities have been estimated from a two-dimensional Gaussian fit to the core component. In this Table we also list the flux densities at 4860 MHz for seven of the sources whose images have been published by MJZK, and also the flux densities for J1313+6937 at 605 and 1425 MHz and for J2312+1845 at 1425 and 4866 MHz from the images published by Konar et al. (2004).

#### 3.1 Notes on the sources

Notes on the overall structure and spectra of the cores are presented in this paper while those based on spectral ages of the lobes are presented in Paper II.

J0720+2837: The eastern lobe has a more prominent hot-spot compared with the western lobe, the ratio of the peak flux density being  $\sim 1.7$ , while the western lobe has more extended emission with the ratio of the total flux density being  $\sim 2.5$  in our 604-MHz image. By convolving the 604-MHz image (Fig. 1) to a similar resolution as that of the VLA 4860-MHz image (MJZK) yields a spectral index,  $\alpha$ , ( $S \propto \nu^{-\alpha}$ ), for the core of 0.63 and 0.59 using the peak and total flux densities respectively estimated from two-dimensional Gaussian fits. The flux densities of the two unrelated sources in the field, the northern one at RA:  $07^{\text{h}} 20^{\text{m}} 13.^{\text{s}}02$ , Dec:  $28^{\circ} 39' 42.''58$ , and the western one at RA:  $07^{\text{h}} 20^{\text{m}} 06.^{\text{s}}09$ , Dec  $28^{\circ} 37' 12.''9$  have also been estimated from the similar-resolution images. All positions are in J2000 co-ordinates. These are 20.1 and 3.3 mJy at 604 and 4860 MHz respectively for the northern source, the corresponding values for the western source being 11.3 and 0.74 mJy. The spectral indices for these sources are 0.87 and 1.31 respectively.

J0912+3510: There is a pair of optical galaxies  $\sim 2.6$  arcsec from the position of the radio core (MJZK), which has a peak brightness of  $\sim 0.4 \text{ mJy beam}^{-1}$  in the 4860-MHz image. It is not certain if either of these galaxies might be associated with the radio source. The core is not unambiguously detected at 606 MHz, the limit being  $\sim 0.6 \text{ mJy beam}^{-1}$  from the full-resolution image. Convolution of the 606-MHz image to that of the 4860-MHz one shows that the central component has a peak brightness of  $0.85 \text{ mJy beam}^{-1}$ , but its position is displaced by  $\sim 14$  arcsec to the north of the core seen in the 4860-MHz image.

J0927+3510: This source has been identified as a possible DDRG by MJZK based on their 4860-MHz VLA image.

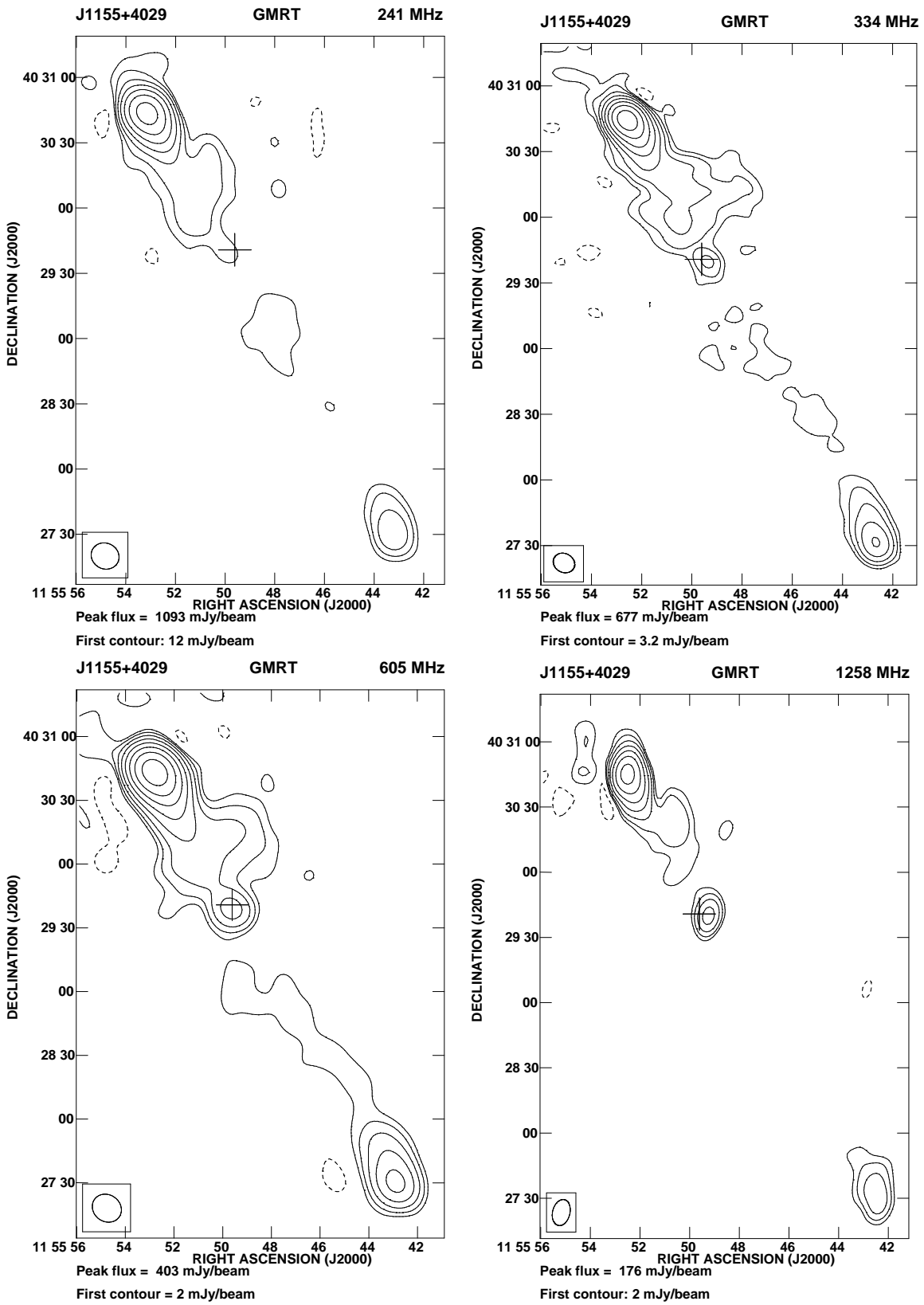


Figure 1 – *continued*

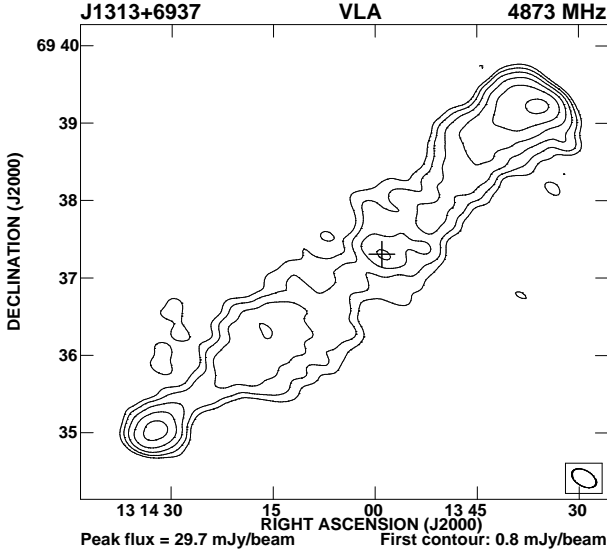


Figure 1 – continued

Our 606-MHz GMRT image also shows clearly the inner components with the optical host galaxy in between. Using the integrated flux densities at 316, 606 and 4860 MHz from images of the same resolution yields spectral indices of  $\sim 1.35$  and  $1.17$  for the inner western and eastern components respectively (see also Paper II). The steep spectral indices suggest that these features are likely to be enhancements in the tail emission rather than a new pair of lobes.

J1155+4029: It is very asymmetric in its arm-length as well as flux density ratios. The arm-length ratio is  $\sim 2.1$ , while the ratios of the peak and total flux densities estimated from the 605-MHz image are  $\sim 14$  and  $7$  respectively with the nearer (eastern) lobe being brighter. The ratios are similar at the other frequencies. In our sample of 10 GRSs, it has the highest value of core fraction of  $0.14$  at a frequency of  $8$  GHz in its rest frame. However, the core has a spectrum which is peaked at  $\sim 1$  GHz (see Section 4.2), and it would be interesting to determine from high-resolution observations whether it might be a mas-scale double.

J1343+3758: This source, which has been studied in some detail by Jamrozny et al. (2005), has an arm-length ratio of  $\sim 1.3$  with the more relaxed (western) lobe being closer to the nucleus. This source has a core with a flat spectrum with  $\alpha \sim 0.1$  between  $604$  and  $4860$  MHz.

J1604+3438: This source was listed as a possible DDRG by MJZK on the basis of their VLA image at  $4860$  MHz. Although higher-resolution observations are required to determine the existence of any hot-spot in the inner structure, the spectral indices of the features which have been suggested to be the inner double are steep. Convolving the GMRT  $1265$ -MHz image to the same resolution as that of the VLA  $4860$ -MHz one, the spectral indices of the western component of the inner structure is  $\sim 1.0$  while for the eastern one  $\alpha \sim 1.8$ . The core spectral index from these images is  $\sim 0.3$ . The steep spectral indices could be affected by contamination with emission from the backflow. Higher resolution images to determine the structure and spectral indices are required to confirm the DDRG nature of the source.

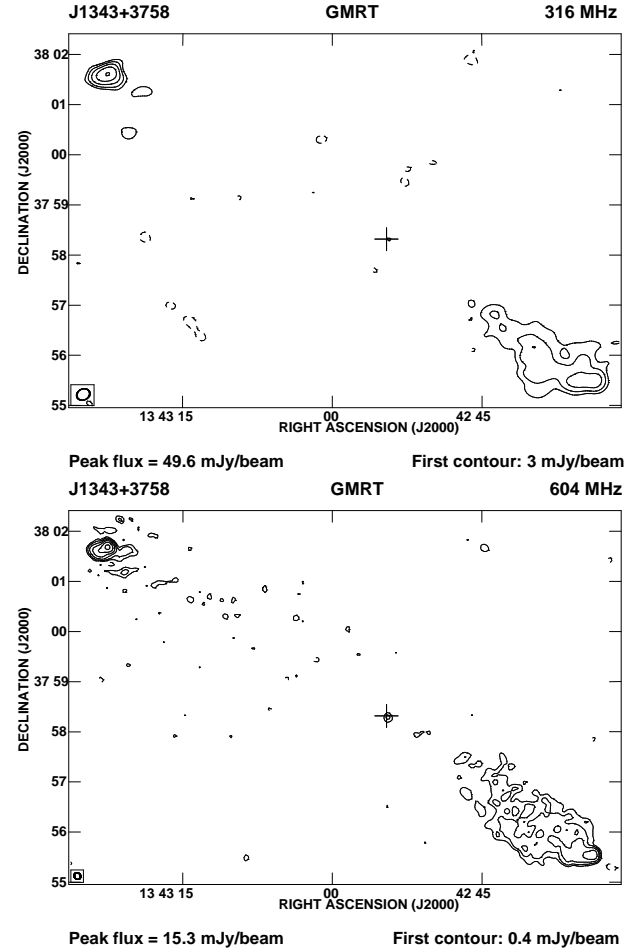


Figure 1 – continued

J1604+3731, 7C: The GMRT  $610$ -MHz image suggests a curved twin-jet structure on opposite sides of the core (Konar et al. 2004). The core is visible in all the GMRT images and in the VLA  $4860$ -MHz and  $9040$  MHz images made from the archival data. The core has a straight steep spectrum with a spectral index of about  $0.76 \pm 0.05$ , which may be due to either small-scale jets and/or lobes not resolved in the existing observations. This needs to be investigated.

J1702+4217, 7C: The core has a flat-spectrum with a spectral index of  $\sim 0.2$  between  $600$  and  $5000$  MHz, and the core flux density rising towards higher frequencies.

J2312+1845, 3C457: The  $334$ -MHz image of the source shows its large scale structure with a barely detected core. The core is contaminated with the diffuse emission of the northern lobe. The core spectral index is  $\sim 0.1$  between  $1425$  and  $4866$  MHz (see Konar et al. 2004).

## 4 DISCUSSION AND RESULTS

Some of the physical properties of the sources are listed in Table 3 which is arranged as follows. Column 1 and 2: source name and an alternative name. Column 3: optical identification where G denotes a galaxy; column 4: redshift; columns 5 and 6: the largest angular size in arcsec and the corresponding projected linear size in kpc; column 7: the lu-

**Table 2.** The observational parameters and observed properties of the sources

Source	Freq. MHz	Beam size			rms mJy beam <sup>-1</sup>	S <sub>I</sub> mJy	C <sub>p</sub>	S <sub>p</sub> mJy beam <sup>-1</sup>	S <sub>t</sub> mJy	C <sub>p</sub>	S <sub>p</sub> mJy beam <sup>-1</sup>	S <sub>t</sub> mJy	C <sub>p</sub>	S <sub>p</sub> mJy beam <sup>-1</sup>	S <sub>t</sub> mJy
(1)	(2)	"	"	°	(6)	(7)	(8)	(9)	(10)	(11)	(12)	(13)	(14)	(15)	(16)
J0720+2837	G604	10.1	9.3	73.3	0.18	96	W	3.2	65	C <sup>g</sup>	2.8	3.3	E	5.3	26
	V4860	19.1	11.9	70	0.03	16	W	1.1	6.7	C <sup>g</sup>	0.85	1.0	E	2.0	7.9
J0912+3510	G334	13.7	12.9	4	0.78	488	N	28	175				S	52	309
	G606	11.8	11.8	0	0.11	257	N	13	82				S	24	171
J0927+3510	V4860	20	20	0	0.04	56	N	5.6	20	C	≲0.4		S	11	36
	G316	20	14.8	98	0.92	376	W	48	160				E	149	214
	G606	12.2	9.6	43	0.11	192	W	20	74				E	74	118
J1155+4029	V4860	22	11.7	73	0.03	27	W	4.5	11	C <sup>g</sup>	0.14	0.14	E	13	16
	G241	13.1	11.8	63	3.24	2120	NE	1087	1774	C	14		SW	96	307
	G334	10.1	8.6	61	1.18	1502	NE	684	1241	C <sup>g</sup>	15	24	SW	54	219
J1313+6937	G605	8.1	4.6	151	0.20	2499	NW	39	1441	C	≲2.0		SE	27	1046
	V1425	14.9	6.5	121	0.10	1383	NW	54	797	C <sup>g</sup>	4.6	7.0	SE	40	585
	V4873	20.4	12.2	60	0.13	431	NW	30	255	C <sup>g</sup>	4.1	4.3	SE	18	172
	G316	16	13.2	117	0.83	455	SW	22	318	C	≲3.0		NE	48	144
J1343+3758	G604	8.4	7.3	29	0.11	253	SW	5.3	165	C <sup>g</sup>	1.0	1.4	NE	15	87
	V4860	15	15	0	0.03	42	SW	3.4	25	C <sup>g</sup>	1.1	1.1	NE	6.7	16
	G239	13.2	11.7	63	1.51	518	W	21	242				E	52	277
J1604+3438	G334	9.8	8.1	81	0.15	510	W	14	241	C	≲2.4		E	35	270
	G614	7.7	5.1	86	0.07	232	W	6.6	108	C	≲1.0		E	14	125
	G1265	7.1	4.5	20	0.07	152	W	3.6	67	C	≲0.5		E	8.6	83
	V4860	15.0	10.0	72	0.06	36	W	2.1	16	C <sup>g</sup>	1.0	1.1	E	6.5	19
	G334	10.4	7.8	68	0.35	522	N	41	222	C <sup>g</sup>	10	12	S	106	284
J1604+3731	G613	7.8	4.8	171	0.10	264	N	14	111	C <sup>g</sup>	5.4	6.4	S	53	142
	G1289	8.3	7.7	26	0.25	144	N	12	61	C <sup>g</sup>	3.8	4	S	32	81
	V4860	13.4	13.1	93	0.01	29	N	4.6	11	C <sup>g</sup>	1.3	1.6	S	10	17
	V9040	7.4	6.7	49	0.01	13	N	1.1	4.2	C <sup>g</sup>	0.9	0.9	S	4.0	7.7
	G602	12.3	4.4	124	0.10	381	NE	30	220	C <sup>g</sup>	1.5	1.9	SW	14	158
J1702+4217	G1288	2.7	2.3	170	0.06	242	NE	7.6	141	C <sup>g</sup>	1.3	1.2	SW	3.8	102
	V4860	13.7	13	65	0.02	48.3	NE	9.7	28	C <sup>g</sup>	1.0	1.3	SW	5.9	19
	V8440	8.8	7.2	63	0.01	23	NE	4.1	14	C <sup>g</sup>	1.4	1.5	SW	1.8	8
	G334	14.1	8.7	85	1.90	8131	NE	954	3510	C	≲18		SW	1089	4537
J2312+1845	V1425	14.2	12.7	179	0.26	1885	NE	311	802	C <sup>g</sup>	3.2	4.1	SW	356	1069
	V4866	14.2	13.7	120	0.12	538	NE	102	230	C <sup>g</sup>	2.9	3.6	SW	123	307

**Table 3.** Physical properties of the sources

Source	Alt. name	Opt. Id.	Redshift	LAS	<i>l</i> kpc	P <sub>1.4</sub> W Hz <sup>-1</sup>	f <sub>c</sub>	R <sub>θ</sub>	R <sub>S</sub>	References
(1)	(2)	(3)	(4)	(5)	(6)	(7)	(8)	(9)	(10)	(11)
J0720+2837		G	0.2705	370	1520	25.02	0.06	1.37	1.06	1
J0912+3510		G	0.2489	375	1449	25.44	≲0.009	1.66	1.82	1
J0927+3510		G	0.55*	345	2206	26.02	0.005	1.02	1.48	1
J1155+4029		G	0.53*	229	1437	26.55	0.14	2.00	0.15	1
J1313+6937	DA 340	G	0.106	388	745	25.60	0.01	1.30	0.68	2,4
J1343+3758		G	0.2267	684	2463	25.32	0.03	1.32	0.63	1,3
J1604+3438		G	0.2817	200	846	25.53	0.04	1.09	1.20	1
J1604+3731	7C	G	0.814	178	1346	26.60	0.04	1.02	0.69	1,5,P
J1702+4217	7C	G	0.476	196	1160	26.20	0.03	1.33	0.69	5,P
J2312+1845	3C457	G	0.427	190	1056	27.11	0.006	1.05	0.75	2

1: Machalski et al. (2006); 2: Konar et al. (2004); 3: Jamrozny et al. (2005); 4: Saunders, Baldwin & Warner (1987); 5: Cotter, Rawlings & Saunders (1996); P: Present paper.

An asterisk in column 4 indicates an estimated redshift.

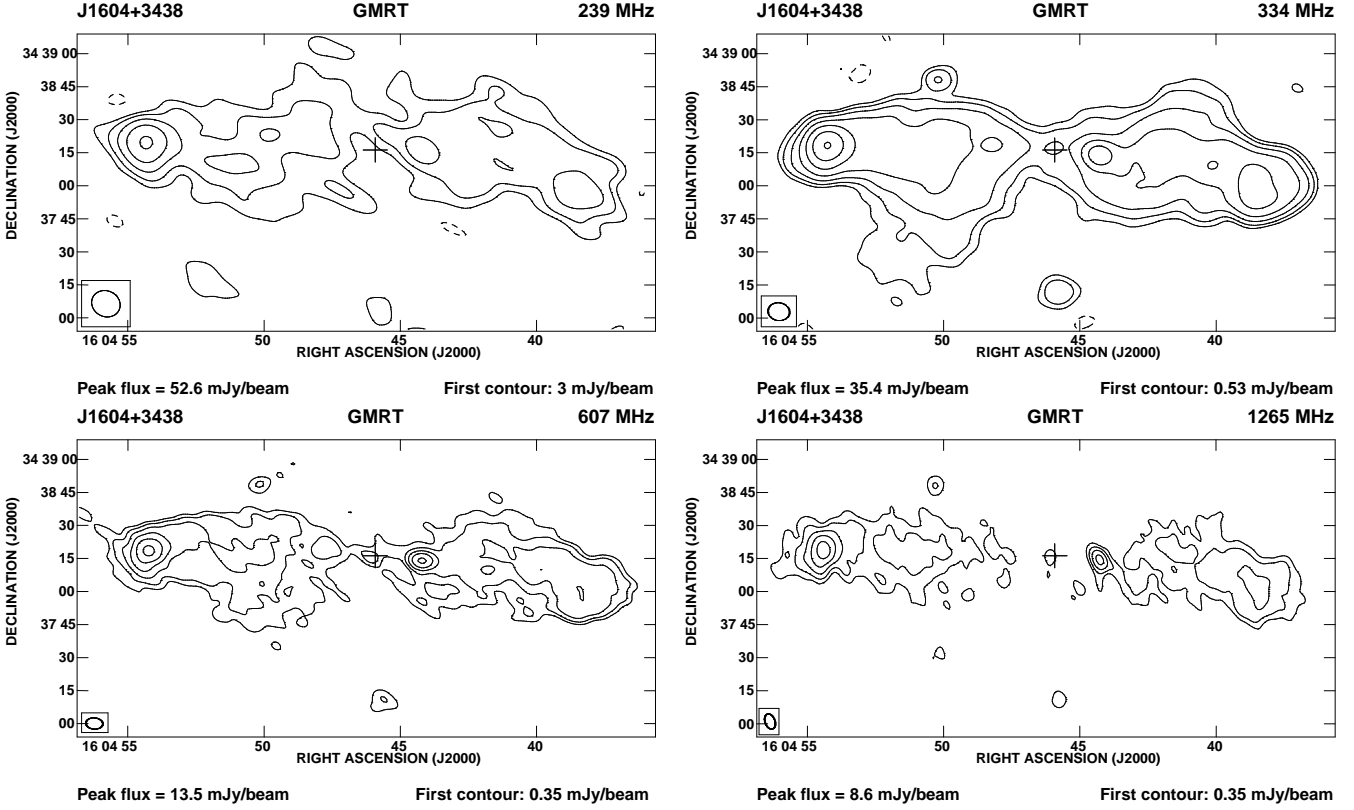


Figure 1 – continued

minosity at 1.4 GHz in logarithmic units of  $\text{W Hz}^{-1}$ ; column 8: the fraction of emission from the core,  $f_c$ , at an emitted frequency of 8 GHz. For estimating  $f_c$ , core spectral indices have been estimated wherever possible, otherwise a value of 0 has been assumed. The separation ratio  $R_\theta$ , defined to be the separation of the farther hotspot or lobe from the core or optical galaxy to the nearer one, and the flux density ratio,  $R_S$  at an emitted frequency of 5 GHz in the same sense, are listed in columns 9 and 10 respectively. References for the radio structure which contains a 5-GHz image and the redshift are listed in column 11. For monochromatic luminosity at 1400 MHz emitted frequency, we have used NVSS images for the total flux density and spectral indices between  $\sim 600$  and 5000 MHz for all sources except J2312+1845 for which we have used the spectral index between  $\sim 1400$  and 5000 MHz.

#### 4.1 Radiative losses

For all the lobes listed in Table 2 we first determine the minimum energy magnetic field strength using the formalism of Miley (1980) by integrating the spectrum between 10 MHz and 100 GHz. We have repeated the calculations by integrating the spectrum from a frequency corresponding to a minimum Lorentz factor,  $\gamma_{\text{min}} \sim 10$  for the relativistic electrons to an upper limit of 100 GHz, which corresponds to a Lorentz factor ranging from a few times  $10^4$  to  $10^5$  depending on the estimated magnetic field strength (see Hardcastle et al. 2004; Croston et al. 2005 and Appendix A). These estimates are referred to as classical-1 and classical-

2 respectively in this paper. The expressions we use for the more general case of a curved radio spectrum in the classical formalisms are described in Appendix A. We also estimate the magnetic field strength,  $B_{\text{eq}}(\text{rev})$ , using the formalism of Beck & Krause (2005) which is an equipartition magnetic field. Their formula (equation A18) has the parameter  $\mathbf{K}_0$  which is the ratio of the number density of protons to that of electrons in the energy range where losses are small. It is relevant to note that in this formalism particle energy is dominated by the protons. Estimating  $\mathbf{K}_0 = (\frac{m_p}{m_e})^\alpha$  as given by their equation (7) for  $\alpha \approx \alpha_{\text{inj}}$  which depends on the low-frequency spectral index in the observed synchrotron spectrum, we can constrain the proton spectrum and hence estimate the revised magnetic field strength,  $B_{\text{eq}}(\text{rev})$ .

We have estimated the magnetic field strengths for the extended lobes of all the sources in our sample using the different approaches, except for J0720+2837 where the spectral coverage is comparatively poor. We have assumed either a cylindrical or spheroidal geometry and a filling factor of unity, and have estimated the sizes of the lobes from the lowest contours in the available low-frequency images at either 330 or 605 MHz. In some sources such as the the eastern lobe of J1343+3758 the emission appears quite compact while in others such as in J1702+4217 there are prominent bridges of emission. The magnetic field in nT ( $1\text{T} = 10^4\text{ G}$ ) estimated from the different approaches as well as the equivalent magnetic field of the cosmic microwave background radiation (CMBR) at the redshift of the source,  $B_{\text{IC}} = 0.32(1+z)^2$  nT, are listed in Table 4, which is self explanatory. A comparison of the magnetic field estimates from the different

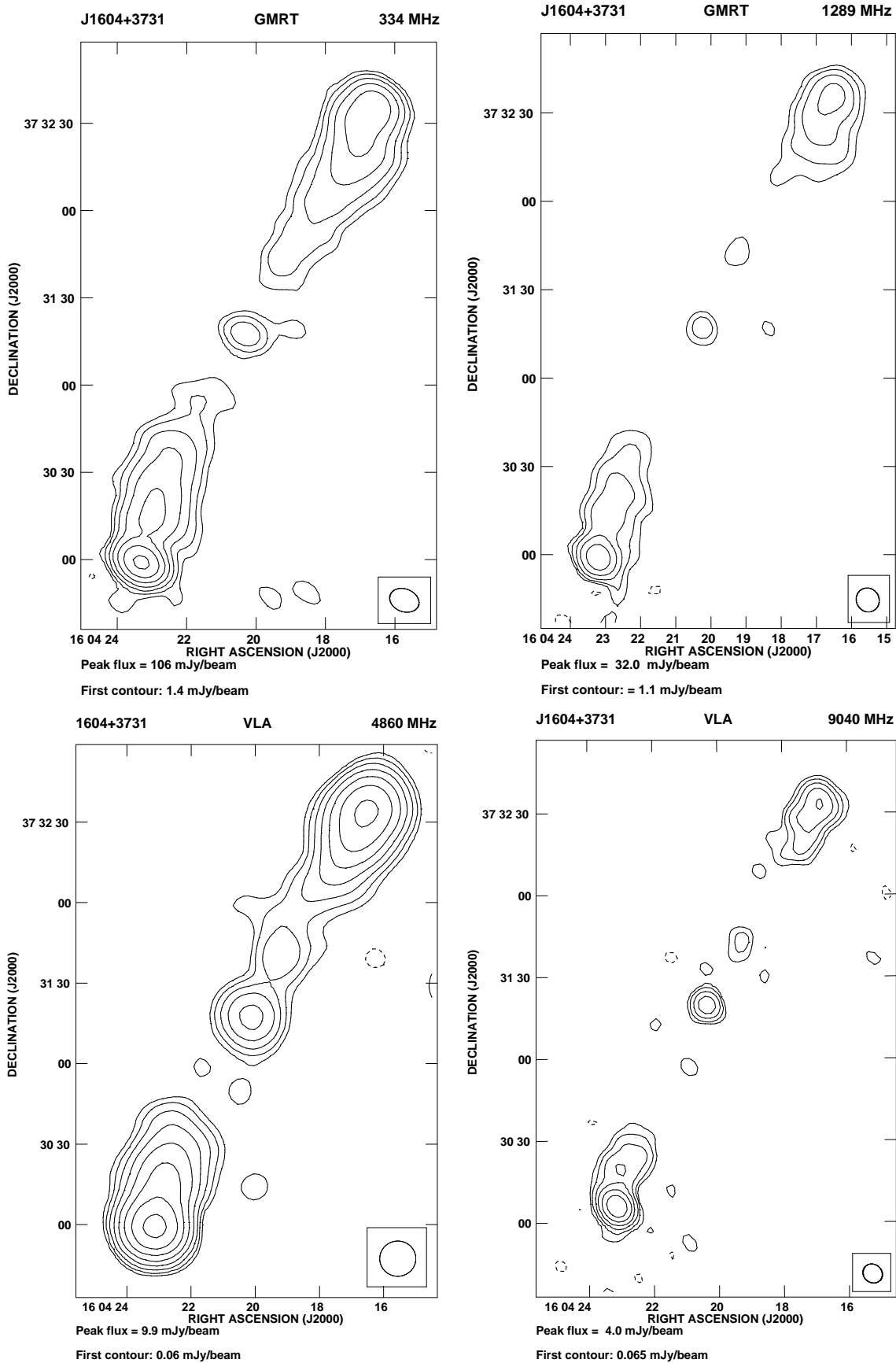


Figure 1 – continued

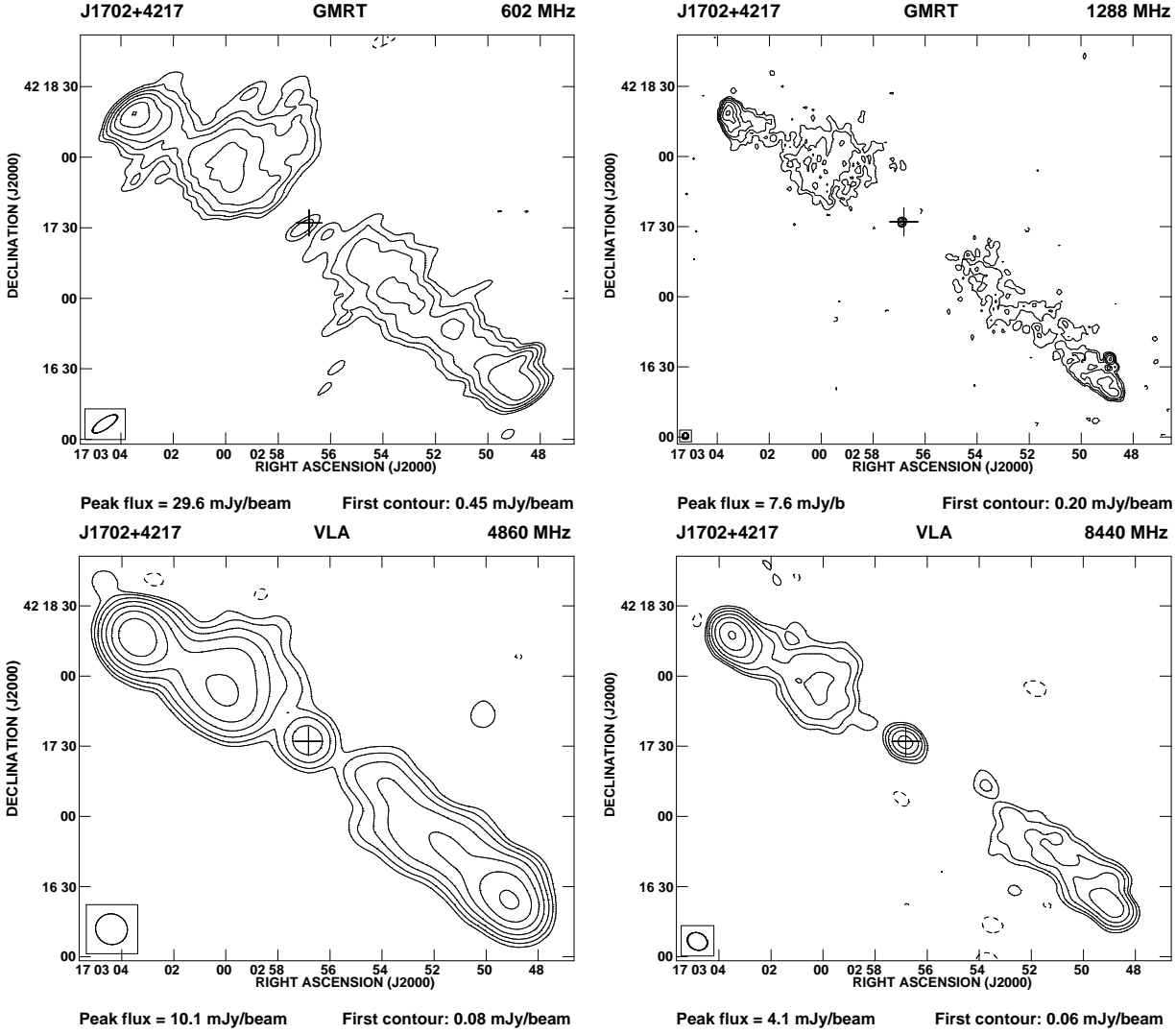


Figure 1 – continued

approaches (Figure 2) shows that the field strengths estimated using the Beck & Krause and classical-2 formalisms are larger than those of classical-1 by factors of  $\sim 3$  and  $\sim 2$  respectively. An independent check of our classical-2 estimates was done by Martin Hardcastle using the formalism of Hardcastle et al. (2004) and the values were found to be consistent.

We examine the relative importance of synchrotron and inverse-Compton losses in the lobes of these radio sources. The ratio of the magnetic field strength estimated from the different approaches to that of the equivalent magnetic field of the CMBR for the different lobes are shown in Fig. 3. It is seen clearly that the magnetic field estimated from the classical-1 approach is always less than  $B_{IC}$ , suggesting that inverse-Compton losses are usually larger than the synchrotron radiative losses for giant radio sources as suggested earlier (e.g. Gopal-Krishna, Wiita & Saripalli 1989; Ishwara-Chandra & Saikia 1999; Konar et al. 2004). The median value of the ratio,  $r_B$ , of the magnetic field estimate to  $B_{IC}$  is  $\sim 0.34$ . However, for the field estimates using the classical-2 and Beck & Krause formalisms the correspond-

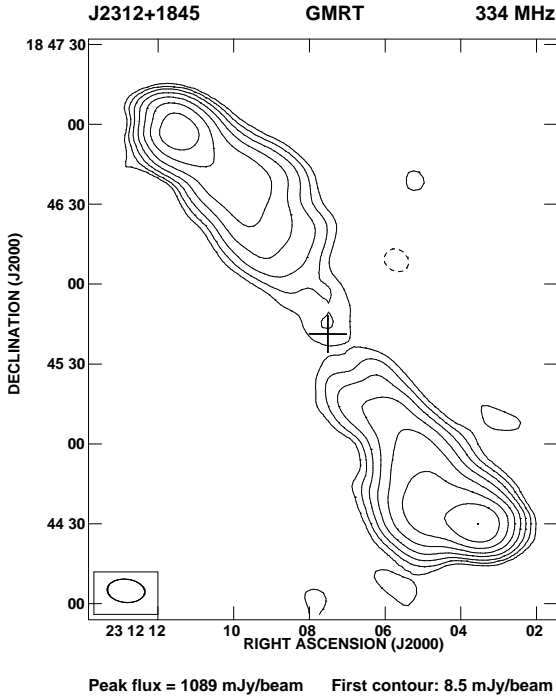
ing values of the ratio  $r_B$  are  $\sim 0.51$  and  $0.91$  respectively. In the latter case, synchrotron losses are more important in approximately half the cases. This could have a significant effect on the identification of GRSs. For example, a combination of increased synchrotron losses combined with the inverse-Compton losses could make it more difficult to detect the bridges of emission in high-redshift GRSs, thereby leading to the classification of the hotspots and a possible core as unrelated radio sources.

## 4.2 Core properties

The fraction of emission from the core at an emitted frequency of 8 GHz,  $f_c$ , ranges from  $\sim 0.005$  to  $0.14$ , with a median value of  $\sim 0.03$ . The values of  $f_c$  are usually comparable to the other sources of similar radio luminosity. The sources with prominent cores ( $f_c \gtrsim 0.04$ ) are J0720+2837, J1155+4029, J1604+3438 and J1604+3731. Of these four sources J0720+2837 has a steep two-point spectral index, J1155+4029 has a giga-Hertz peaked spectrum (GPS) core, J1604+3438 has a flat-spectrum core while J1604+3731 has

**Table 4.** Magnetic field estimates of the lobes

Source	Comp.	Magnetic field estimates					Equivalent CMB field
		JP: class-1 nT	JP: class-2 nT	KP: class-1 nT	KP: class-2 nT	Beck-Krause nT	
(1)	(2)	(3)	(4)	(5)	(6)	(7)	(8)
J0912+3510	N	0.11±0.01	0.16±0.02	0.11±0.01	0.16±0.02	0.34±0.05	0.50
	S	0.13±0.01	0.21±0.02	0.13±0.01	0.21±0.02	0.39±0.05	
J0927+3510	NW	0.13±0.01	0.27±0.03	0.13±0.01	0.27±0.03	0.38±0.05	0.77
	SE	0.14±0.01	0.25±0.02	0.14±0.01	0.25±0.02	0.35±0.04	
J1155+4029	NE	0.50±0.05	1.15±0.11	0.50±0.05	1.13±0.11	1.52±0.18	0.75
	SW	0.32±0.03	0.70±0.07	0.31±0.03	0.68±0.07	0.99±0.12	
J1313+6937	NW	0.19±0.02	0.29±0.03	0.19±0.02	0.29±0.03	0.60±0.08	0.39
	SE	0.15±0.01	0.23±0.02	0.15±0.01	0.23±0.02	0.48±0.06	
J1343+3758	SW	0.13±0.01	0.23±0.02	0.13±0.01	0.23±0.02	0.40±0.05	0.48
	NE	0.20±0.02	0.33±0.03	0.20±0.02	0.32±0.03	0.60±0.08	
J1604+3438	W	0.17±0.02	0.24±0.02	0.17±0.02	0.24±0.02	0.52±0.07	0.53
	E	0.20±0.02	0.28±0.03	0.20±0.02	0.28±0.03	0.60±0.08	
J1604+3731	N	0.26±0.03	0.52±0.05	0.26±0.03	0.51±0.05	0.58±0.07	1.05
	S	0.37±0.04	0.73±0.07	0.37±0.04	0.72±0.07	0.83±0.10	
J1702+4217	NE	0.20±0.02	0.30±0.03	0.20±0.02	0.30±0.03	0.48±0.06	0.70
	SW	0.20±0.02	0.30±0.03	0.20±0.02	0.30±0.03	0.47±0.06	
J2312+1845	NE	0.40±0.04	0.86±0.08	0.40±0.04	0.85±0.08	1.23±0.15	0.65
	SW	0.43±0.04	0.91±0.09	0.43±0.04	0.90±0.09	1.32±0.16	

**Figure 1** – *continued*

a steep spectrum core from  $\sim 300$  to 9000 MHz (see Section 3.1). The flux densities of the cores of J1155+4029 and J1604+3731 where multiple measurements are available are listed in Tables 5 and 6 respectively along with the approximate resolution and the epoch of observations, and their spectra are presented in Fig. 4. For sources where contamination of core emission by diffuse extended emission at the lower frequencies seem significant, the source has been remapped with a lower uv-cutoff of 5  $k\lambda$  to minimise

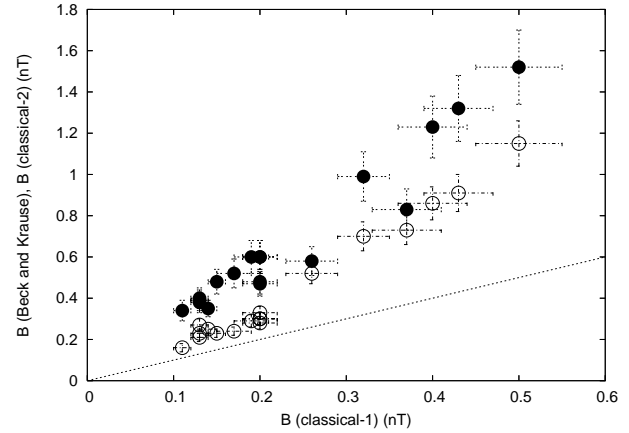


**Figure 2.** The magnetic field strength estimated using the formalisms of Beck & Krause (2005) shown by filled circles and classical-2 (see text and Croston et al. 2005) shown by open circles are plotted against the classical-1 estimates (see text and Miley 1980). The dotted line represents field strengths estimated using the Beck & Krause and classical-2 formalisms being equal to the classical-1 estimates.

contamination by the extended emission. It would be interesting to determine from mas-scale resolution observations whether the core of J1155+4029 is resolved into a pc-scale double. It is worth mentioning that the GPS core of the GRS, J1247+6723, is resolved into a small-scale double with a size of  $\sim 14$  pc, suggesting recurrent activity (Marecki et al. 2003; Saikia, Konar & Kulkarni 2006). It is also relevant to note that the core does not exhibit any evidence of significant variability as in the case of other GPS sources (e.g. O’Dea 1998 for a review). For example the core flux densities from the FIRST survey at 1400 MHz and our GMRT 1258-MHz image are similar even though they are temporally far apart.

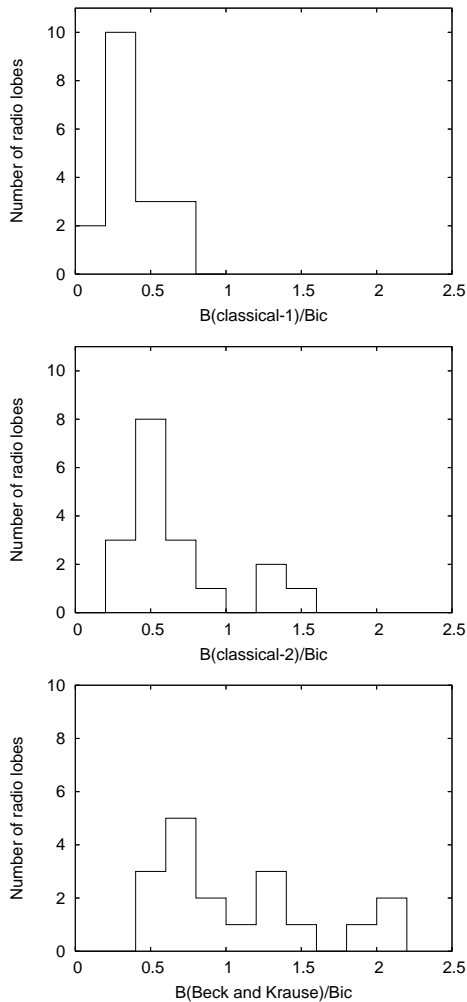


**Figure 3.** The distributions of the ratios of the magnetic field strength estimated using the classical-1, classical-2 and Beck & Krause (2005) formalisms and the equivalent magnetic field,  $B_{IC}$ , of the CMBR, shown in the upper, middle and lower panels respectively.

### 4.3 Environment and morphology of GRSs

The lobes of the GRSs lie well beyond the extent of the parent host galaxies and can be used to probe the environment on these scales which could affect the structure and symmetry parameters of these objects (e.g Subrahmanyan et al. 1996). Although GRSs often occur in regions of low galaxy density, Subrahmanyan et al. noted that two of the sources in their sample, namely B1545–321 and B2356–611, which have continuous bridges from the hotspots to the core show significant excesses in galaxy counts. Ishwara-Chandra & Saikia (1999) and Schoenmakers et al. (2000) noted that the GRSs tended to be marginally more asymmetric than smaller sources of similar luminosity, excluding the compact steep spectrum sources. For example, considering the higher luminosity objects Ishwara-Chandra & Saikia noted that the median value of the separation ratio is  $\sim 1.39$  compared with  $\sim 1.19$  for 3CR galaxies of similar luminosity but smaller sizes. The median value for these ten sources in our sample is  $\sim 1.31$  (see Fig. 5, upper panel), consistent with the earlier estimate although the statistical uncertainties are now

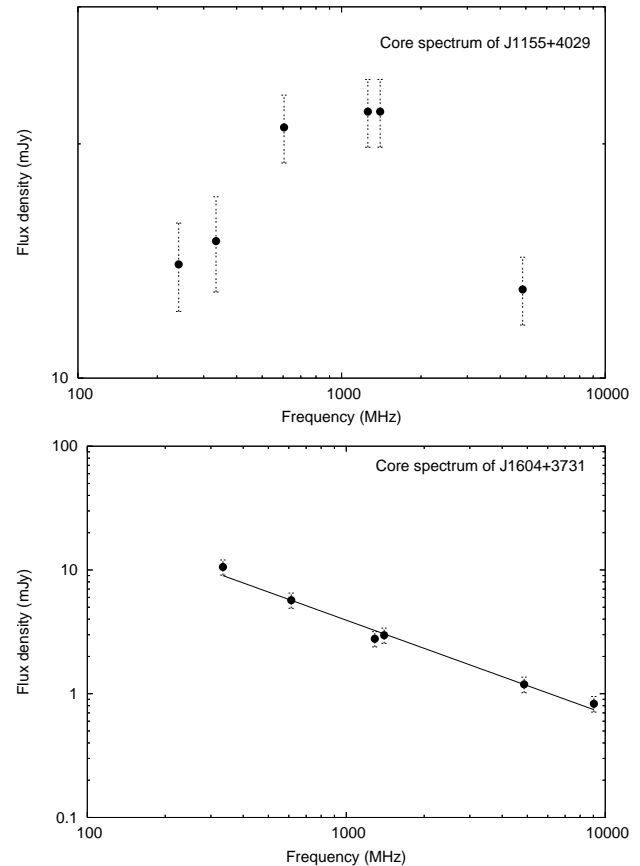


**Figure 4.** Upper panel: core spectrum of J1155+4029; lower panel: a least-square fit of a power-law to the core spectrum of J1604+3731.

larger because of the small sample size. The distribution does not show a significant peak towards smaller values. For a source inclined at  $\gtrsim 45^\circ$  to the line of sight, the expected separation ratio is only  $\sim 1.15$  for a hotspot advance speed of  $\sim 0.1c$  (see Scheuer 1995). A plot of the separation ratio against the fraction of emission from the core (Fig. 5, upper panel), which is often used as a statistical indicator of orientation of the source axis to the line of sight, shows no significant correlation suggesting that large-scale environmental asymmetries play a significant role. It is worth noting that although J1155+4029, which has the most prominent core, and has the highest value of the separation ratio, the nearer component is brighter by a factor of  $\sim 6$  (Fig. 5, lower panel), demonstrating that density asymmetries are likely to again play a significant role in the observed asymmetries. It is also relevant to note that the radio source J1155+4029 which has the highest value of  $f_c=0.14$  has a GPS core; it is important to determine its structure with mas resolution and investigate whether it might be a compact double with a rather weak core.

Although flux density ratios would be affected by relative contributions of the hotspot and backflow emission which have different velocities, in addition to effects of evolution of individual components with age, it can be seen in Fig. 5 (middle and lower panels) that in 6 of the 10 sources the nearer component is brighter as is expected if their jets are going through a denser medium (e.g. Jeyakumar et al.

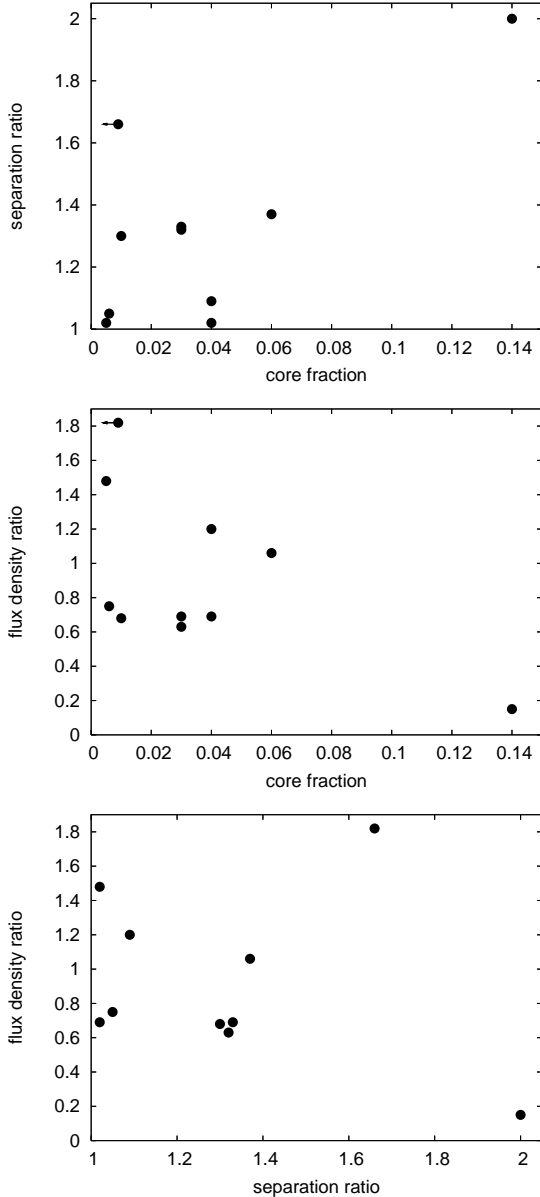


**Figure 5.** The separation ratios and flux density ratios are plotted against the fraction of emission from the core at an emitted frequency of 8 GHz in the upper and middle panels respectively. In the lower panel the flux density ratio is plotted against the separation ratio.

2005). In spite of the difficulties noted above, weak trends for the components on the jet side in quasars to be stronger have been reported (e.g Garrington, Conway & Leahy 1991), illustrating that relativistic effects also play a role. However, in these giant radio sources, environmental effects seem to dominate, with the flux density ratio too exhibiting no significant dependence on core prominence (Fig. 5, middle panel). It would be interesting to explore the fields of these sources both via optical galaxy counts and deep x-ray observations, and examine their relationships with the observed structures.

**Table 5.** Core flux densities of J1155+4029

Teles-cope (1)	resn." (2)	Date (3)	Freq. MHz (4)	S mJy (5)	Ref. (6)
GMRT	9.9	2005 Mar 16	241	14	1
GMRT	9.3	2005 Dec 25	334	15	1
GMRT	6.1	2005 Mar 16	605	21	1
GMRT	9.9	2005 Nov 30	1258	22	1
VLA-B	5.4	FIRST	1400	22	2
VLA-D	14.7	2004 Jul 31	4860	13	1

1: Present paper; 2: FIRST

**Table 6.** Core flux densities of J1604+3731

Teles-cope (1)	resn." (2)	Date (3)	Freq. MHz (4)	S mJy (5)	Ref. (6)
GMRT	7.2	2006 Mar 09	334	10.6	1
GMRT	5.1	2004 Jan 01	613	5.7	1
GMRT	3.5	2006 Jan 01	1289	2.8	1
VLA-BnD	5.4	FIRST	1400	3.0	2
VLA-D	10.6	1993 Dec 23	4860	1.2	1
VLA-D	6.6	1993 Dec 23	9040	0.8	1

1: Present paper; 2: FIRST

## 5 CONCLUDING REMARKS

We have presented multifrequency radio images of a selected sample of ten giant radio galaxies, largely at low radio frequencies with the GMRT. We have also presented a few high-frequency images made from VLA data. We have listed the flux densities of components for the images presented here as well as for high-frequency images of these sources which have been published earlier by us (MJZK; Konar et al. 2004).

From these multifrequency observations of the lobes we estimate the magnetic field strengths using three different approaches, namely estimating the minimum energy field by integrating from 10 MHz to 100 GHz which has been referred to here as classical-1 (Miley 1980), integrating from a minimum frequency corresponding to  $\gamma_{\min}=10$  at the estimated magnetic field to a maximum frequency of 100 GHz, called classical-2 (see Hardcastle et al. 2004; Croston et al. 2005), and lastly using the formalism of Beck & Krause (2005). We show that on the average the magnetic field strengths estimated using the Beck & Krause and classical-2 formalisms are larger than the classical-1 values by factors of  $\sim 3$  and  $\sim 2$  respectively.

The inverse-Compton losses dominate over synchrotron losses when estimates of the classical minimum energy magnetic field are used, consistent with earlier studies. However, this is often not true if the magnetic fields are close to the values estimated using the formalism of Beck & Krause (2005). In the latter case, synchrotron losses are more important in nearly half the cases. The increased synchrotron losses combined with the inverse-Compton losses would make it more difficult to detect the bridges of emission in high-redshift GRSs, thereby leading to the classification of the hotspots and a possible core as unrelated radio sources. Although for a sample of radio galaxies with x-ray emission from at least one of the lobes which can be attributed to

inverse Compton scattering with the CMBR photons, the estimated magnetic field ranges from  $\sim 0.3$  to 1.3 times the minimum energy field with a peak around 0.7 times this field (Croston et al. 2005), none of the radio lobes in clusters of galaxies studied by Dunn, Fabian & Taylor (2005) has equipartition between the relativistic particles and the magnetic field. Clearly more work is required in this area.

We also examine the spectral indices of the cores and any evidence of recurrent activity in these sources. In one of the sources, J1155+4029, the core has a GPS spectrum, while in two others, J0720+2837 and J1604+3731, the cores appear to have a steep spectrum. It would be interesting to determine the milliarcsec-scale structure of the core in J1155+4029 as well as J0720+2837 and J1604+3731 and thereby examine whether these show evidence of being a double double radio galaxy.

We probe the environment using the symmetry parameters of these sources. Approximately half the sources are more asymmetric in their separation ratio than would be expected for a galaxy inclined at  $\gtrsim 45^\circ$  to the line of sight with the hotspots moving outwards with a velocity of  $\sim 0.1c$ . Also the nearer lobe is brighter in six of the sources, the asymmetry being most pronounced in the case of J1155+4029 which has the largest value of separation ratio and a GPS core. These trends suggest that the environments of these sources are often asymmetric on scales of  $\sim 1$  Mpc, consistent with earlier studies.

## ACKNOWLEDGMENTS

We thank Martin Hardcastle for his advice and comments and for making an independent check of our classical-2 estimates using the formalism of Hardcastle et al. (2004). We also thank Rainer Beck, Gopal-Krishna, Martin Krause, Vasant Kulkarni, Paul Wiita and an anonymous referee for their comments on the manuscript. The Giant Metrewave Radio Telescope is a national facility operated by the National Centre for Radio Astrophysics of the Tata Institute of Fundamental Research. We thank the staff for help with the observations. The National Radio Astronomy Observatory is a facility of the National Science Foundation operated under co-operative agreement by Associated Universities Inc. We thank the VLA staff for easy access to the archival data base. This research has made use of the NASA/IPAC extragalactic database (NED) which is operated by the Jet Propulsion Laboratory, Caltech, under contract with the National Aeronautics and Space Administration. We thank numerous contributors to the GNU/Linux group.

## REFERENCES

Baars J.W.M., Genzel R., Pauliny-Toth I.I.K., Witzel A. 1977, *A&A*, 61, 99  
 Beck R., Krause M., 2005, *AN*, 326, 414  
 Becker R.H., White R.L., Helfand D.J., 1995, *ApJ*, 450, 559  
 Blundell, K.M., Rawlings, S., Willott, C.J., 1999, *AJ*, 117, 677  
 Condon J.J., Cotton W.D., Greisen E.W., Yin Q.F., Perley R.A., Taylor G.B., Broderick J.J., 1998, *AJ*, 115, 1693  
 Cotter G., Rawlings S., Saunders R., 1996, *MNRAS*, 281, 1081  
 Croston J.H., Hardcastle M.J., Harris D.E., Belsole E., Birkinshaw M., Worrall D.M., 2005, *ApJ*, 626, 733

Dunn R.J.H., Fabian A.C., Taylor G.B., 2005, *MNRAS*, 364, 1343  
 Garrington S.T., Conway R.G., Leahy J.P., 1991, *MNRAS*, 250, 171  
 Gopal-Krishna, Wiita P.J., Saripalli L., 1989, *MNRAS*, 239, 173  
 Hardcastle M.J., Harris D.E., Worrall D.M., Birkinshaw M., 2004, *ApJ*, 612, 729  
 Ishwara-Chandra C.H., Saikia D.J., 1999, *MNRAS*, 309, 100  
 Jaffe W.J., Perola G.C., 1973, *A&A*, 26, 423  
 Jamroz M., Machalski J., Mack K.-H., Klein U., 2005, *A&A*, 433, 467  
 Jamroz M., Konar C., Machalski J., Saikia D.J., 2007, *MNRAS*, submitted (Paper II)  
 Jeyakumar S., Wiita P.J., Saikia D.J., Hooda J.S., 2005, *A&A*, 432, 823  
 Kaiser C.R., Alexander P. 1999, *MNRAS*, 302, 515  
 Kardashev N.S., 1962, *SvA*, 6, 317  
 Konar C., Saikia D.J., Ishwara-Chandra C.H., Kulkarni V.K., 2004, *MNRAS*, 355, 845  
 Konar C., Saikia D.J., Jamroz M., Machalski, 2006, *MNRAS*, 372, 693  
 Law-Green J.D.B., Eales S.A., Leahy J.P., Rawlings S., Lacy M., 1995, *MNRAS*, 277, 995  
 Machalski J., Jamroz M., Zola S., 2001, *A&A*, 371, 445  
 Machalski J., Jamroz M., Zola S., Koziel D., 2006, *A&A*, 454, 85 (MJZK)  
 Machalski J., Chyży K.T., Stawarz L., Koziel D., 2007, *A&A*, 462, 43  
 Mack K.-H., Klein U., O’Dea C. P., Willis A. G., Saripalli L., 1998, *A&A*, 329, 431  
 Marecki A., Barthel P.D., Polatidis A., Owsianik I., 2003, *PASA*, 20, 16  
 Miley G. K., 1980, *ARA&A*, 18, 165  
 Murgia M., 1996, Laurea Thesis, University of Bologna  
 Myers S.T., Spangler S.R., 1985, *ApJ*, 291, 52  
 O’Dea C.P., 1998, *PASP*, 110, 493  
 Pacholczyk A.G., 1970, *Radio Astrophysics*, W.H. Freeman, San Francisco  
 Saikia D.J., Konar C., Kulkarni V.K., 2006, *MNRAS*, 366, 1391  
 Saunders R., Baldwin J.E., Warner P.J., 1987, *MNRAS*, 225, 713  
 Scheuer P.A.G., 1995, *MNRAS*, 277, 331  
 Schoenmakers A.P., 1999, PhD Thesis, Rijksuniversiteit Groningen  
 Schoenmakers A.P., Mack K.-H., de Bruyn A.G., Röttgering H.J.A., Klein U., van der Laan H., 2000, *A&AS*, 146, 293  
 Schoenmakers A.P., de Bruyn A.G., Röttgering H.J.A., van der Laan H., 2001, *A&A*, 374, 861  
 Spergel D.N. et al., 2003, *ApJS*, 148, 175  
 Strom R.G., Willis A.G., 1980, *A&A*, 85, 36  
 Subrahmanyan R., Saripalli L., 1993, *MNRAS*, 260, 908  
 Subrahmanyan R., Saripalli L., Hunstead R.W., 1996, *MNRAS*, 279, 257

## APPENDIX A: ESTIMATING CLASSICAL EQUIPARTITION MAGNETIC FIELD

In this paper we estimate the magnetic field using the revised equipartition method (Beck & Krause 2005) as well as the widely used classical minimum energy approach summarised by Miley (1980) and also a variant of this method which is described below. The latter two approaches are referred to as classical-1 and classical-2 in this paper. Since the expressions in the literature for the classical-1 approach are for a power law spectrum, and many of the GRSSs show evidence of curvature in the integrated spectrum, we estimate the magnetic field by numerically integrating over the non power-law spectrum.

To derive a general formula for the minimum energy magnetic field for non power-law spectra we proceed as follows. The equations used are summarised here. The critical frequency at which an electron of energy  $E$  radiates most of its energy is given by

$$\nu = C_1 B (\sin\phi) E^2 \quad (\text{A1})$$

where  $C_1 = 6.266 \times 10^{18}$  in cgs units, and is a constant (Pacholczyk 1970). The energy loss of a single electron is given by

$$-\frac{dE}{dt} = C_2 B^2 (\sin^2\phi) E^2 \quad (\text{A2})$$

where  $C_2 = 2.368 \times 10^{-3}$  in cgs units, is also a constant (Pacholczyk 1970)

Let us assume that the number of electrons between  $E$  and  $E + dE$  is given by  $N(E)dE$ . They will radiate via synchrotron emission between  $\nu$  and  $\nu + d\nu$ , where  $\nu$  and  $E$  are related by the equation (A1). The monochromatic luminosity,  $L(\nu)$ , is given by

$$L(\nu)d\nu = N(E)dE \times \left(-\frac{dE}{dt}\right) \quad (\text{A3})$$

Substituting the value of  $-\frac{dE}{dt}$  from equation (A2) we get

$$N(E)dE = \frac{C_1}{C_2} \frac{1}{B \sin\phi} \frac{L(\nu)}{\nu} d\nu \quad (\text{A4})$$

The total kinetic energy of the electrons is given by

$$U_e = \int EN(E)dE = \frac{1}{B^{3/2} \sin^{3/2}\phi} C_4 \int \frac{L(\nu)}{\sqrt{\nu}} d\nu \quad (\text{A5})$$

$E$  has been substituted from equation (A1) and  $C_4 = \frac{\sqrt{C_1}}{C_2}$  is  $1.05709 \times 10^{12}$  in cgs units.

The above expression can be re-written as

$$U_e = \frac{A}{B^{3/2} \sin^{3/2}\phi} \quad (\text{A6})$$

where

$$A = C_4 \int \frac{L(\nu)}{\sqrt{\nu}} d\nu \quad (\text{A7})$$

Assuming the proton to electron energy density ratio to be  $\kappa$  we get the total energy expression as

$$U_{tot} = (1 + \kappa)U_e + U_B = \frac{(1 + \kappa)A}{B^{3/2} \sin^{3/2}\phi} + V \frac{B^2}{8\pi} \quad (\text{A8})$$

Differentiating  $U_{tot}$  with respect to  $B$  and equating  $\frac{dU_{tot}}{dB}$  to zero we get the minimum energy expression

$$B_{min} = \left(\frac{6\pi A(1 + \kappa)}{V \sin^{3/2}\phi}\right)^{2/7} \quad (\text{A9})$$

where  $A$  is given by equation (A7), while  $V$  and  $L(\nu)$  can be written as follows.

$V = \eta f_s \frac{d_A^2 \theta_x'' \theta_y'' s}{(206265)^2}$ , and  $L(\nu) = 4\pi d_L^2 S(\nu)$  Here,  $\eta$  is the filling factor,  $f_s$  is a shape factor for the volume of the emission region, which assumes a value of  $\frac{\pi}{4}$  for a cylinder and  $\frac{\pi}{6}$  for an ellipsoid,  $d_A$  and  $d_L$  are angular-diameter and luminosity distances respectively,  $\theta_x''$  and  $\theta_y''$  are the two projected dimensions of the emission region,  $s$  is the depth of the emission region.

So far, all  $\nu$  and  $S(\nu)$  values are in emitter's frame. Converting them into the quantities of observer's frame and expressing the quantities in practical units we get

$$B_{min}(\mu G) = 10^6(1+z) \left[ \frac{3.26604 \times 10^{-32}}{\sin^{3/2}\phi} \frac{(1 + \kappa)A'}{\eta f_s \theta_x'' \theta_y'' s (kpc)} \right]^{2/7} \quad (\text{A10})$$

Here  $A' = C_4 \int_{\nu_1^o}^{\nu_2^o} \frac{S_{mJy}^o(\nu^o)}{\sqrt{\nu_{MHz}^o}} d\nu_{MHz}^o$ . The superscript 'o' indicates that the quantities are in the observer's frame. The integration should be carried out within a frequency interval which is compatible with the emitter's frame frequency interval set by us.  $(2/3)^{3/4}$  has been substituted for  $\sin^{3/2}\phi$  in the above equation to estimate  $B_{min}$ , as the average value of  $\sin^2\phi = \frac{2}{3}$ .

As a first step, we fit the observed flux density measurements with the spectral ageing models of Jaffe & Perola (1973, hereinafter referred to as JP) as well as Kardashev (1962) and Pacholczyk (1970), hereinafter referred as KP, with the help of the SYNAGE package (Murgia 1996), and then extrapolate to very low and high frequencies. For the integration limits, we first use the range 10 MHz – 100 GHz in the emitter's frame for the classical-1 approach. For classical-2 we set the integration limit such that the lower limit corresponds to a Lorentz factor,  $\gamma_{min}$  of  $\sim 10$  while the upper limit corresponds to 100 GHz, as in classical-1 (see Myers & Spangler 1985; Hardcastle et al. 2004; Croston et al. 2005). Since, we don't have an independent estimate of the magnetic field to start with, we assume a lower limit, say, 10 MHz to start with, keeping the upper limit fixed at 100 GHz. Then we calculate the magnetic field and check what value of  $\gamma_{min}$  does the lower limit of frequency correspond to using the relation  $\nu = C_1 B \sin\phi (\gamma - 1)^2 m_e c^2$ , where  $m_e$  is the rest mass of the electron and  $c$  represents the velocity of light. Then we vary the lower limit iteratively till we get  $\gamma_{min}$  close to 10.